Simulation of anisotropic wave propagation based upon a spectral element method

Dimitri Komatitsch*, Christophe Barnes‡, and Jeroen Tromp*

ABSTRACT

We introduce a numerical approach for modeling elastic wave propagation in 2-D and 3-D fully anisotropic media based upon a spectral element method. The technique solves a weak formulation of the wave equation, which is discretized using a high-order polynomial representation on a finite element mesh. For isotropic media, the spectral element method is known for its high degree of accuracy, its ability to handle complex model geometries, and its low computational cost. We show that the method can be extended to fully anisotropic media. The mass matrix obtained is diagonal by construction, which leads to a very efficient fully explicit solver. We demonstrate the accuracy of the method by comparing it against a known analytical solution for a 2-D transversely isotropic test case, and by comparing its predictions against those based upon a finite difference method for a 2-D heterogeneous, anisotropic medium. We show its generality and its flexibility by modeling wave propagation in a 3-D transversely isotropic medium with a symmetry axis tilted relative to the axes of the grid.

INTRODUCTION

Geological media often exhibit complex features such as curved interfaces with strong impedance contrasts, faults, and surface topography that are difficult to incorporate in numerical simulations of elastic wave propagation. Furthermore, such media are often seismically anisotropic, for instance as a result of fractured rocks, fluid-filled cracks (Crampin et al., 1984), or thin isotropic layering (Backus, 1962). In global seismology, anisotropy plays an important role in 1-D reference models, such as PREM (Dziewonski and Anderson, 1981), as well as for surface waves propagating along oceanic paths (Forsyth, 1975).

Calculating seismic waveforms in complex geological structures is a challenging task for most classical methods. For a homogeneous medium with a high degree of symmetry (e.g., transverse isotropy), one can use analytic or semi-analytic solutions (e.g., White, 1982; Payton, 1983). Wave propagation in an anisotropic layer-cake model can be described based upon the reflectivity method (Booth and Crampin, 1983) or equivalent media theory (Schoenberg and Muir, 1989). But for the general case of a heterogeneous, fully anisotropic medium one needs to turn to numerical methods such as finite difference (FD) (e.g., Igel et al., 1995) and pseudospectral (e.g., Tessmer, 1995) techniques.

One of the main difficulties with the FD method in the context of general anisotropic media is the fact that some interpolation of the components of the strain tensor is needed to determine the components of the stress tensor, due to the use of staggered grids (Igel et al., 1995). The lowest degree of symmetry that can be modeled without interpolation is the orthorhombic case with axes aligned with those of the computational grid. An additional problem with FD methods is related to the implementation of the free surface boundary condition (Robertsson, 1996), which is approximate and therefore leads to difficulties in the representation of surface waves.

Fourier methods are very accurate within the model volume as long as the velocity model considered is smooth (Carcione et al. 1988, 1992). Unfortunately, the implementation of accurate boundary conditions is very difficult due to the periodic nature of the Fourier expansion (Kosloff et al., 1984). Nonperiodic basis functions (e.g., Chebychev polynomials) were introduced to alleviate some of these difficulties (Tessmer, 1995). However, this approach involves a 1-D treatment at the free surface in order to stabilize the stress-free boundary condition (e.g., Carcione and Wang, 1993; Komatitsch et al., 1996),

which reduces the accuracy of the surface waves. Furthermore, as with the Fourier method, the use of a global basis leads to inaccuracies in the wave field for models with strong heterogeneity or sharp boundaries.

The spectral element method (SEM) was introduced by Patera (1984) in computational fluid dynamics. It was first used for modeling seismic wave propagation by Seriani et al. (1992), and has been successfully applied to 2-D and 3-D problems related to elastic, isotropic media (e.g., Priolo et al., 1994; Komatitsch, 1997; Faccioli et al., 1997; Komatitsch and Vilotte 1998; Seriani, 1998; Komatitsch and Tromp, 1999; Komatitsch et al., 1999). The method has also been successfully applied to problems involving both fluid and solid regions (Komatitsch et al., 2000). The main attributes of the SEM are its ability to handle models with steep free-surface topography, a highly accurate representation of surface and refracted waves, and its computational efficiency, in particular on parallel computers.

In this paper, we extend the SEM to the most general case of 3-D fully anisotropic media with 21 independent elastic coefficients. The Legendre formulation used in this article leads to a mass matrix that is exactly diagonal by construction, therefore resulting in a very efficient fully explicit solver, which is a very significant advantage over classical finite element methods. The 2-D transversely-isotropic case with a symmetry axis aligned with the vertical axis of the grid was studied previously by Seriani et al. (1995) using a variant of the SEM based on a Chebyshev formulation leading to a nondiagonal mass matrix. This 2-D case is obtained here as a particular case of the general 3-D formulation with diagonal mass matrix. We validate the approach by comparing it against an analytical solution for a 2-D homogeneous, transversely isotropic model, and by comparing it against a FD solution for a 2-D heterogeneous, anisotropic model. We show its efficiency and its flexibility by studying a 3-D homogeneous model consisting of a transversely-isotropic medium whose symmetry axis is tilted with respect to the axes of the grid. We again obtain excellent agreement with the analytical solution on the symmetry axis.

ANISOTROPIC WAVE EQUATION

In a heterogeneous elastic, anisotropic medium, the linear wave equation may be written as

$$
\begin{aligned}
\rho \ddot{\mathbf{u}} &= \nabla \cdot \boldsymbol{\sigma} + \mathbf{f}, \\
\boldsymbol{\sigma} &= \mathbf{C} : \varepsilon, \\
\varepsilon &= \tfrac{1}{2}[\nabla \mathbf{u} + (\nabla \mathbf{u})^T],
\end{aligned}
\tag{1}
$$

where $\mathbf{u}$ denotes the displacement vector, $\boldsymbol{\sigma}$ the symmetric, second-order stress tensor, ε the symmetric, second-order strain tensor, $\mathbf{C}$ the fourth-order stiffness tensor, ρ the density, and $\mathbf{f}$ an external source force. A dot over a symbol denotes time differentiation, a colon denotes the tensor product, and a superscript T denotes the transpose.

In the case of a fully anisotropic medium, the 3-D stiffness tensor $\mathbf{C}$ has 21 independent components. In 2-D, the number of independent components reduces to 6. Using the reduced Voigt notation (see e.g., Helbig, 1994), Hooke's law may be

written in the form

$$
\begin{pmatrix}
\sigma_{xx} \\
\sigma_{yy} \\
\sigma_{zz} \\
\sigma_{yz} \\
\sigma_{xz} \\
\sigma_{xy}
\end{pmatrix}
=
\begin{pmatrix}
c_{11} & c_{12} & c_{13} & c_{14} & c_{15} & c_{16} \\
c_{21} & c_{22} & c_{23} & c_{24} & c_{25} & c_{26} \\
c_{31} & c_{32} & c_{33} & c_{34} & c_{35} & c_{36} \\
c_{41} & c_{42} & c_{43} & c_{44} & c_{45} & c_{46} \\
c_{51} & c_{52} & c_{53} & c_{54} & c_{55} & c_{56} \\
c_{61} & c_{62} & c_{63} & c_{64} & c_{65} & c_{66}
\end{pmatrix}
\begin{pmatrix}
\varepsilon_{xx} \\
\varepsilon_{yy} \\
\varepsilon_{zz} \\
2\varepsilon_{yz} \\
2\varepsilon_{xz} \\
2\varepsilon_{xy}
\end{pmatrix}.
\tag{2}
$$

Using this reduced notation, the stiffness matrix remains symmetric, i.e., $c_{IJ} = c_{JI}$. The isotropic case is obtained by letting $c_{11} = c_{22} = c_{33} = \lambda + 2\mu$, $c_{12} = c_{13} = c_{23} = \lambda$, and $c_{44} = c_{55} = c_{66} = \mu$, where λ and μ are the two Lamé parameters; all other coefficients are then equal to zero.

In the case of a medium with free surfaces (e.g., the edges of a crystal or the surface of the earth), the boundary condition is zero traction at the surface: $\boldsymbol{\sigma} \cdot \hat{\mathbf{n}} = \mathbf{0}$, where $\hat{\mathbf{n}}$ is the unit outward normal vector. The reader is referred to Crampin et al. (1984), Thomsen (1986), or Helbig (1994) for further details on wave propagation in anisotropic media.

SPECTRAL ELEMENT APPROXIMATION

In a spectral element approach, the strong form of the equations of motion (1) is first rewritten in a variational or weak formulation. This is accomplished by dotting it with an arbitrary test vector $\mathbf{w}$ and integrating by parts over the region of interest (e.g., Hughes, 1987), which gives

$$
\begin{aligned}
\int_{\Omega} \rho \mathbf{w} \cdot \ddot{\mathbf{u}} \, d\Omega &+ \int_{\Omega} \nabla \mathbf{w} : \mathbf{C} : \nabla \mathbf{u} \, d\Omega \\
&= \int_{\Omega} \mathbf{w} \cdot \mathbf{f} \, d\Omega + \int_{\Gamma_{\text{abs}}} \mathbf{w} \cdot \mathbf{t} \, d\Gamma.
\end{aligned}
\tag{3}
$$

Here Ω denotes the physical region of interest. Its boundary Γ can consist in two parts: a boundary Γ_f on which free surface conditions are implemented, and an artificial boundary Γ_{abs} on which absorbing conditions have to be implemented. In the integration by parts, we have used the fact that the traction vanishes on the free boundaries Γ_f of the domain. Therefore, a free surface condition is naturally implemented in a SEM. In the isotropic case, simple approximate absorbing conditions can be implemented on Γ_{abs} by using dampers to express the traction as a function of the velocity field and of the model impedances (Clayton and Engquist, 1977; Komatitsch and Vilotte, 1998). Higher-order, and therefore more precise, conditions can also be used (Quarteroni et al., 1998), but are more difficult to implement. As pointed out in Komatitsch and Tromp (1999), the idea of Clayton and Engquist (1977) can still be used for transversely isotropic media. For more general anisotropy, such as the general case considered in this paper, the easiest solution is to taper the elastic properties such that the medium becomes transversely isotropic on the artificial boundary.

The Legendre spectral element discretization of the variational problem (3) proceeds as follows. A mesh of n_{el}

nonoverlapping quadrangles in two dimensions, or hexahedra in three dimensions, Ω_e, is defined on the domain Ω, as in a classical finite element method (FEM). These elements are subsequently mapped to a reference domain $\Lambda = [-1, 1]^{n_d}$ (a square in two dimensions, $n_d = 2$; a cube in three dimensions, $n_d = 3$) using an invertible local mapping $\mathcal{F}_e : \Lambda \rightarrow \Omega_e$, which enables one to go from the physical domain to the reference domain, and vice versa.

On the reference domain Λ, we introduce a set of local basis functions consisting of polynomials of degree N. On each element Ω_e, mapped to the reference domain Λ, we define a set of nodes, and choose the polynomial approximation $\mathbf{u}_N^e$ and $\mathbf{w}_N^e$ of $\mathbf{u}$ and $\mathbf{w}$ to be the Lagrange interpolant at this set of nodes. These nodes $\xi_i \in [-1, 1]$, $i \in 0, \ldots, N$, are the Gauss-Lobatto-Legendre (GLL) points which are the $(N+1)$ roots of

$$(1 - \xi^2)P_N'(\xi) = 0, \qquad (4)$$

where $P_N'(\xi)$ is the derivative of the Legendre polynomial of degree N. On the reference domain Λ, the restriction of a given function u_N to the element Ω_e can be expressed as

$$u_N^e(\xi, \eta, \gamma) = \sum_{p=0}^{N} \sum_{q=0}^{N} \sum_{r=0}^{N} u_N^e(\xi_p, \eta_q, \gamma_r) h_p(\xi) h_q(\eta) h_r(\gamma), \qquad (5)$$

where $h_p(\xi)$ denotes the pth 1-D Lagrange interpolant at the $(N+1)$ GLL points ξ_i introduced above, which is by definition the unique polynomial of degree N that is equal to one at $\xi = \xi_p$ and to zero at all other points $\xi = \xi_q$ for which $q \neq p$. From this definition, we obtain the fundamental property

$$h_p(\xi_q) = \delta_{pq}. \qquad (6)$$

Once we have invoked the piecewise-polynomial approximation (5), the integrals in equation (3) can be approximated at the element level using the GLL integration rule:

$$\int_{\Omega} u_N w_N \, d\Omega = \sum_{e=1}^{n_{el}} \int_{\Omega_e} u_N^e w_N^e \, d\Omega$$

$$\simeq \sum_{e=1}^{n_{el}} \sum_{i=0}^{N} \omega_i \sum_{j=0}^{N} \omega_j \sum_{k=0}^{N} \omega_k J_e(\xi_i, \eta_j, \gamma_k) u_N^e$$

$$\times (\xi_i, \eta_j, \gamma_k) w_N^e(\xi_i, \eta_j, \gamma_k). \qquad (7)$$

The weights $\omega_i > 0$, which are independent of the element, are determined numerically (Canuto et al., 1988, p. 61), and J_e is the Jacobian associated with the mapping $\mathcal{F}_e$ from the element Ω_e to the reference domain Λ.

The discrete variational problem that has to be solved is therefore as follows: for all times t, find $\mathbf{u}_N$ such that for all test vectors $\mathbf{w}_N$ we have

$$\langle \mathbf{w_N}, \rho \ddot{\mathbf{u}}_N \rangle + a(\mathbf{w}_N, \mathbf{u}_N) = \langle \mathbf{w}_N, \mathbf{f}_N \rangle. \qquad (8)$$

Here we have defined

$$\langle \mathbf{w}_N, \rho \ddot{\mathbf{u}}_N \rangle = \sum_{e=1}^{n_{el}} \sum_{i=0}^{N} \omega_i \sum_{j=0}^{N} \omega_j \sum_{k=0}^{N} \omega_k J_e^{ijk} \rho_e^{ijk} \mathbf{w}_{e,N}^{ijk} \cdot \ddot{\mathbf{u}}_{e,N}^{ijk},$$

$$a(\mathbf{w}_N, \mathbf{u}_N) = \sum_{e=1}^{n_{el}} \sum_{i=0}^{N} \omega_i \sum_{j=0}^{N} \omega_j$$

$$\times \sum_{k=0}^{N} \omega_k J_e^{ijk} \boldsymbol{\nabla} \mathbf{w}_{e,N}^{ijk} : \mathbf{C}_e^{ijk} : \boldsymbol{\nabla} \mathbf{u}_{e,N}^{ijk}, \qquad (9)$$

$$\langle \mathbf{w}_N, \mathbf{f}_N \rangle = \sum_{e=1}^{n_{el}} \sum_{i=0}^{N} \omega_i \sum_{j=0}^{N} \omega_j \sum_{k=0}^{N} \omega_k J_e^{ijk} \mathbf{w}_{e,N}^{ijk} \cdot \mathbf{f}_{e,N}^{ijk},$$

where $\rho_e^{ijk} = \rho_e(\xi_i, \eta_j, \gamma_k)$, $\mathbf{w}_{e,N}^{ijk} = \mathbf{w}_{e,N}(\xi_i, \eta_j, \gamma_k)$, etc. Gradients are first computed in the reference domain Λ:

$$\partial_\xi u_N^e(\xi, \eta, \gamma) = \sum_{p=0}^{N} \sum_{q=0}^{N} \sum_{r=0}^{N}$$
$$\times u_N^e(\xi_p, \eta_q, \gamma_r) h_p'(\xi) h_q(\eta) h_r(\gamma),$$

$$\partial_\eta u_N^e(\xi, \eta, \gamma) = \sum_{p=0}^{N} \sum_{q=0}^{N} \sum_{r=0}^{N}$$
$$\times u_N^e(\xi_p, \eta_q, \gamma_r) h_p(\xi) h_q'(\eta) h_r(\gamma),$$

$$\partial_\gamma u_N^e(\xi, \eta, \gamma) = \sum_{p=0}^{N} \sum_{q=0}^{N} \sum_{r=0}^{N}$$
$$\times u_N^e(\xi_p, \eta_q, \gamma_r) h_p(\xi) h_q(\eta) h_r'(\gamma). \qquad (10)$$

where h' denotes the derivative of the 1-D Lagrange interpolant. We subsequently use the chain rule to compute the derivatives in the physical domain, i.e., $\partial_x = \xi_x \partial_\xi + \eta_x \partial_\eta + \gamma_x \partial_\gamma$, $\partial_y = \xi_y \partial_\xi + \eta_y \partial_\eta + \gamma_y \partial_\gamma$, $\partial_z = \xi_z \partial_\xi + \eta_z \partial_\eta + \gamma_z \partial_\gamma$, where the components of the Jacobian matrix, ξ_x, ξ_y, ξ_z etc. . . are computed based upon the mapping $\mathcal{F}_e$.

MODELING ANISOTROPY

The effects of anisotropy are represented by the term $a(\mathbf{w}_N, \mathbf{u}_N)$ in equation (8); all other terms are identical to those in an isotropic formulation (see e.g., Komatitsch and Vilotte, 1998; Komatitsch and Tromp, 1999). This anisotropic term can be rewritten as

$$a(\mathbf{w}_N, \mathbf{u}_N) \simeq \int_{\Omega} \boldsymbol{\sigma}(\mathbf{u}_N) : \boldsymbol{\nabla} \mathbf{w}_N \, d\Omega. \qquad (11)$$

Written out explicitly, the integrand is given by

$$\boldsymbol{\sigma}(\mathbf{u}_N) : \boldsymbol{\nabla} \mathbf{w}_N = \sigma_{ij} \partial_j w_i. \qquad (12)$$

In the fully anisotropic 3-D case, using the definition $\varepsilon_{ij} = (\partial_i u_j + \partial_j u_i)/2$ and Hooke's law (2), equation (12) involves a sum of terms of the form $c_{\alpha\beta} \partial_a u_b \partial_c w_d$, with $c_{\alpha\beta}$ the components of the reduced stiffness matrix (2).

Each of the terms in this expression, integrated over an element Ω_e, is easily computed by substituting the expansion of the fields (5), computing gradients using equations (10) and the chain rule, and using the GLL integration rule (7). As an

example, let us consider the first term in that developed expression. We have

$$\int_{\Omega_e} c_{11} \partial_x u_x^e \partial_x w_x^e \, \mathrm{d}\Omega \simeq \sum_{i=0}^{N} \omega_i \sum_{j=0}^{N} \omega_j \sum_{k=0}^{N} \omega_k J_e^{ijk} c_{11}^{ijk}$$

$$\times \left[\xi_x^{ijk} \sum_{p=0}^{N} h_p'(\xi_i) \sum_{q=0}^{N} h_q(\eta_j) \sum_{r=0}^{N} u_{xe}^{pqr} h_r(\gamma_k) \right.$$

$$+ \eta_x^{ijk} \sum_{p=0}^{N} h_p(\xi_i) \sum_{q=0}^{N} h_q'(\eta_j) \sum_{r=0}^{N} u_{xe}^{pqr} h_r(\gamma_k)$$

$$\left. + \gamma_x^{ijk} \sum_{p=0}^{N} h_p(\xi_i) \sum_{q=0}^{N} h_q(\eta_j) \sum_{r=0}^{N} u_{xe}^{pqr} h_r'(\gamma_k) \right]$$

$$\times \left[\xi_x^{ijk} \sum_{r=0}^{N} h_r'(\xi_i) \sum_{s=0}^{N} h_s(\eta_j) \sum_{t=0}^{N} w_{xe}^{rst} h_t(\gamma_k) \right.$$

$$+ \eta_x^{ijk} \sum_{r=0}^{N} h_r(\xi_i) \sum_{s=0}^{N} h_s'(\eta_j) \sum_{t=0}^{N} w_{xe}^{rst} h_t(\gamma_k)$$

$$\left. + \gamma_x^{ijk} \sum_{r=0}^{N} h_r(\xi_i) \sum_{s=0}^{N} h_s(\eta_j) \sum_{t=0}^{N} w_{xe}^{rst} h_t'(\gamma_k) \right] \quad (13)$$

which, using the fundamental property (6), reduces to

$$\int_{\Omega_e} c_{11} \partial_x u_x^e \partial_x w_x^e \, \mathrm{d}\Omega \simeq \sum_{i=0}^{N} \omega_i \sum_{j=0}^{N} \omega_j \sum_{k=0}^{N} \omega_k J_e^{ijk} c_{11}^{ijk}$$

$$\times \left[\xi_x^{ijk} \sum_{p=0}^{N} u_{xe}^{pjk} h_p'(\xi_i) + \eta_x^{ijk} \sum_{q=0}^{N} u_{xe}^{iqk} h_q'(\eta_j) \right.$$

$$\left. + \gamma_x^{ijk} \sum_{r=0}^{N} u_{xe}^{ijr} h_r'(\gamma_k) \right] \left[\xi_x^{ijk} \sum_{r=0}^{N} w_{xe}^{rjk} h_r'(\xi_i) \right.$$

$$\left. + \eta_x^{ijk} \sum_{s=0}^{N} w_{xe}^{isk} h_s'(\eta_j) + \gamma_x^{ijk} \sum_{t=0}^{N} w_{xe}^{ijt} h_t'(\gamma_k) \right]. \quad (14)$$

After this spatial discretization with spectral elements, imposing that equation (8) holds for *any* test vector $\mathbf{w}_N$, as in a classical FEM, we have to solve an ordinary differential equation in time. Denoting by U the global vector of unknown displacement in the medium, we see that we can rewrite equation (8) in matrix form as

$$M\ddot{U} + KU = F, \quad (15)$$

where M is traditionally called the mass matrix, K the stiffness matrix, and F the source term. A very important property of the SEM used here, which allows for a drastic reduction in the complexity and the cost of the algorithm, is the fact that the mass matrix M is diagonal as a consequence of the choice of Lagrange interpolants at the GLL points in conjunction with the GLL integration rule. This is shown for instance in Komatitsch and Vilotte (1998), and constitutes a major difference compared to a classical FEM, or to variants of the SEM based on a Chebyshev formulation, as introduced by Seriani et al. (1992) and Priolo et al. (1994).

Time discretization of the second-order ordinary differential equation in time (15) is achieved using a classical explicit Newmark scheme (Hughes, 1987, chap. 9), which is second-order accurate and conditionally stable. We assume zero initial condi-

tions ($U = 0$ and $\dot{U} = 0$ at $t = 0$) that are easily implemented as initial displacement and velocity fields in the Newmark scheme. It is worth mentioning here that in a SEM, the spatial discretization is very accurate since it is based on high-degree polynomials. To the contrary, the time discretization used here is only second-order accurate, therefore reducing the global accuracy of the scheme, and in this respect it could be of interest to use higher-order time schemes, for instance based on the work of Tarnow and Simo (1994).

2-D ANISOTROPIC CRYSTALS

In order to validate the method, we first study 2-D homogeneous, anisotropic crystals in the ultrasonic frequency range, motivated by a previous study of the same problem based upon the Fourier method (Carcione et al., 1988) and by the 2-D results obtained by Seriani et al. (1995) using a variant of the SEM based upon Chebyshev polynomials. These results, as well as the analytical solution, are used for comparison. We consider two crystals: apatite and zinc (whose elastic properties are summarized in Table 1). These crystals are homogeneous and transversely isotropic; for simplicity in this first test, we choose the axis of symmetry of the crystal to coincide with the vertical axis of the grid. The case of a tilted axis will be studied for a 3-D medium in the next section.

In the simulations, the size of the crystals is 33 cm × 33 cm, and all their boundaries are free surfaces. A vertical point force is applied exactly at the center of the domain. The source time function is a Ricker wavelet (i.e., the second derivative of a Gaussian) with dominant frequency f_0 chosen in the ultrasonic frequency range. Due to the very different elastic properties of the two crystals, f_0 is taken to be 300 kHz in the case of apatite and 170 kHz in the case of zinc. The onset time of the source is $t_0 = 6 \, \mu$s. The medium is discretized using a grid of $50 \times 50 = 2500$ spectral elements, and a polynomial degree $N = 5$ is used within each element. Thus each element contains $(N + 1)^2 = 36$ points, and the total number of grid points is 63 001. The number of spectral elements is chosen such that the resolution is close to 5 grid points per minimum qS wavelength along the slowest axis of the crystal. Because the test involves a comparison with a reference solution, we choose a small time step in the explicit second-order Newmark scheme in order to be sure that the contribution of the time integration error is small. We use a time step of 50 ns and propagate the waves for 110 μs (i.e., 2200 time steps).

Snapshots of the displacement vector in the crystals are shown in Figure 1 at times $t = 20 \, \mu$s for apatite and $t = 32 \, \mu$s for zinc. The two simulations exhibit strong anisotropy, with typical curved quasilongitudinal (qP) and quasitransversal (qS) modes

Table 1. **Elastic properties and density of the two 2-D transversely isotropic crystals used in the validation tests, in the case of a symmetry axis aligned with the vertical axis of the grid. The elastic coefficients have to be multiplied by 10^{10} to obtain values in N·m^{-2}. The densities ρ are given in kg·m^{-3}. The other elastic coefficients are zero for these crystals.**

Crystal	c_{11}	c_{13}	c_{33}	c_{55}	ρ
Apatite	16.7	6.6	14.0	6.63	3200.
Zinc	16.5	5.0	6.2	3.96	7100.

(note the very anisotropic qP wavefront in zinc for instance), and typical cuspidal triangles. We have superimposed the theoretical wavefronts for the qP and qS modes (dashed curves), whose analytical expression can be found in Payton (1983) and in Carcione et al. (1988). Our simulations reproduce the expected shape of the wavefronts very well, including the cusps of the qS mode (very clear in the case of apatite). The snapshots are also in good qualitative agreement with similar simulations performed by Carcione et al. (1988) using a Fourier method (Figures 3 and 4 of their article). The SEM results do not exhibit significant noise nor numerical oscillations.

In order to take advantage of analytical expressions for the displacement along the symmetry axis (Payton, 1983), we placed two receivers in the crystal exactly above the source at distances of 3.3 cm and 9.9 cm, respectively. The numerical and the analytical solution are shown together in Figure 2 for apatite. Since the two curves are almost superimposed, we also plot the difference between them amplified by a factor of 5. The agreement between the two solutions is excellent at both receivers.

In Figure 3, we show the two components of displacement recorded in the zinc crystal by a horizontal line of 50 receivers situated at a distance of 9.9 cm above the source, between $x_{r_1} = 5$ cm and $x_{r_{50}} = 28$ cm (this line of receivers is indicated by dots in Figure 1). We clearly see the direct qP and qS waves, as well as reflections and conversions that occur at the free surfaces on all four boundaries of the crystal. The direct qS wave exhibits a clear cusp close to the center of the receiver line (i.e., just above the source), in agreement with the theoretical wavefronts shown in Figure 1.

2-D HETEROGENEOUS, ANISOTROPIC MODEL

To further validate the method, and show that it is able to handle a heterogeneous medium, we consider the case of a model composed of two half-spaces: a transversely isotropic zinc crystal with vertical symmetry axis on the left, identical to that used in the previous section, and an isotropic material on the right. This 2-D problem has been studied previously by Carcione et al. (1988) using a Fourier method. The isotropic medium is chosen to be close to an "isotropic" version of zinc, i.e., its P-wave velocity corresponds to the qP-wave velocity of zinc along the horizontal axis, and its S-wave velocity corresponds to the qS-wave velocity of zinc. The mechanical properties of the anisotropic and isotropic materials are summarized in Table 2. The source is a vertical point force located 2 cm to the left of the interface in the anisotropic half-space. The source time function is a Ricker wavelet with dominant frequency $f_0 = 170$ kHz and onset time $t_0 = 6\,\mu$s. A horizontal line of receivers is located 8 cm below the source and is composed of 49 recorders, one every 5 mm from $x_r = -12$ cm to $+12$ cm relative to the interface. The geometry of the experiment is illustrated in Figure 4. Absorbing conditions are used on the four edges of the grid in order to simulate two half-spaces in contact.

For a quantitative comparison, we perform a FD calculation that is used as a reference. We use a standard staggered FD scheme that is fourth order in space and second order in time. No additional interpolation is needed in such a scheme for transversely isotropic media with respect to the isotropic case. Spatial resolution is purposely chosen to be very fine in order to
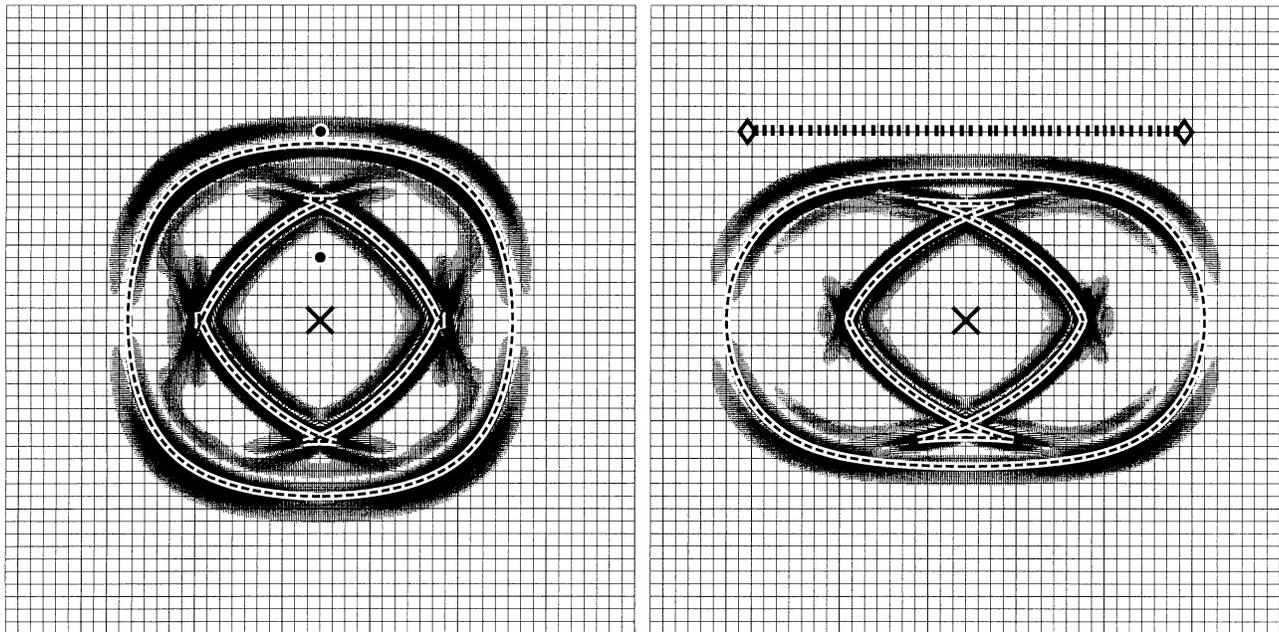
FIG. 1. Snapshots of the displacement vector in two transversely isotropic crystals: apatite at time $t = 20\,\mu$s (left), and zinc at time $t = 32\,\mu$s (right). The source is a vertical point force applied in the middle of the crystal, indicated by a cross. The mesh represents the $50 \times 50 = 2500$ spectral elements of degree $N = 5$. Both crystals exhibit strong anisotropy, with a curved qP wavefront (very strongly curved for zinc) and a qS wavefront with cuspidal triangles. The analytical wavefronts (dashed lines) have been superimposed and are in very good agreement with our simulation. The two dots for apatite indicate the position of the two receivers used in Figure 2. The dotted line for zinc indicates the line of receivers used to record the seismograms of Figure 3.

compute a very precise reference for comparison with the SEM results. The medium is therefore discretized using a grid spacing of 0.5 mm. The domain has a size of 68 cm × 64 cm; therefore the global grid contains 1361×1281 points. The simulation uses 4000 time steps of 25 ns for the same reason. A snapshot of the vertical component of displacement at time $t = 60\,\mu s$ is shown in Figure 4.

In the SEM simulation, a 65 cm × 65 cm region is discretized using a much coarser grid of $130 \times 130 = 16\,900$ spectral elements and a polynomial degree $N = 5$. Therefore the average number of grid points per minimum wavelength in the model is close to 6, and the size of the "equivalent" global grid is 651×651 points. As pointed out in Faccioli et al. (1997), in a SEM, due to the fact that polynomials of high degree are used for the spatial discretization, a high accuracy is attained by using a relatively small number of grid points per wavelength. This means that, from the point of view of computational cost, SEMs compare very well with widely used techniques such as high-order FD methods.

The simulation uses 2000 time steps of 50 ns. A snapshot of the displacement at time $t = 32\,\mu s$ is shown in Figure 5. Displacement is recorded at the same 49 receivers as in the FD simulation. A seismogram of the vertical component is plotted in the upper part of Figure 6. This seismogram is compared to the FD results, and residuals, amplified by a factor of 5, are shown in the lower part of Figure 6. The agreement is excellent. In Figures 4–6, numerous phases can be identified. The main ones are summarized in Table 3. For most of the phases, the following naming convention has been used. The first letter indicates the mode (P/S) of the incoming wave. In the anisotropic medium, the P and S waves are in fact qP and qS. A letter "i" indicates an interaction with the interface; a letter "r" denotes refraction as a P-wave along the interface, since the vertical P-wave speed is higher in the isotropic part of the

Table 2. **Mechanical properties of the elastic materials used in the numerical experiment with a 2-D heterogeneous medium. The c_{IJ} are expressed in 10^{10} N·m^{-2}. The density ρ is expressed in kg·m^{-3}. The other elastic coefficients are zero.**

	c_{11}	c_{13}	c_{33}	c_{55}	ρ
Anisotropic	16.50	5.00	6.20	3.96	7100.
Isotropic	16.50	8.58	16.50	3.96	7100.

FIG. 2. Numerical (solid line) and analytical (dashed line) vertical component of displacement recorded at two receivers located on the symmetry axis of the apatite crystal at distances of 3.3 cm (top) and 9.9 cm (bottom) above the source. The position of the receivers is indicated by dots in Figure 1. Because the two curves are almost superimposed, the difference between them, amplified by a factor of 5, is also plotted (dotted line). The horizontal component of displacement, which is zero on the symmetry axis, is not displayed.

FIG. 3. Horizontal (top) and vertical (bottom) components of displacement recorded in the zinc crystal at the line of receivers shown in Figure 1. Both seismograms show the direct qP wavefront and the direct qS wavefront with a clear cusp. In addition, numerous phases reflected and converted on the four boundaries (free surfaces) of the crystal are recorded. The seismograms do not exhibit significant noise nor numerical oscillations except for some small numerical dispersion around the main cusp of the direct qS wavefront.

medium. The last letter indicates the mode (P/S) of the outgoing wave. Lowercase letters refer to transmitted waves in the isotropic medium; uppercase letters refer to reflected waves in the anisotropic medium.

In Figure 7, for four receivers located at $x_r = -10.5$ cm, -3.5 cm, -1 cm, and $+10.5$ cm, the individual SEM traces are compared to the FD results, and the residuals, amplified by a factor of 5, are also plotted. The agreement is excellent, except perhaps for the SiS phase. Note that there is a very small time shift for several phases, and that residuals for waves transmitted in the isotropic domain are systematically smaller. This can be explained by the well-known fact that the position of the interface in the FD method is not clearly defined because of the use of a staggered grid. This induces a time delay that is larger for reflected than for transmitted waves.

3-D TRANSVERSELY ISOTROPIC MEDIUM WITH TILTED AXIS

To show the generality of the method and demonstrate its flexibility, we study the case of a 3-D transversely isotropic medium with a symmetry axis tilted with respect to the axes of the computational grid. We wish to validate the method for a case in which most of the 21 elastic coefficients are nonzero. We could use a general triclinic medium, but the 3-D transversely isotropic case presents the big advantage that, for some materials and in the case of a force source, the displacement can be computed analytically along the symmetry axis (Carcione et al., 1992, Appendix A), therefore providing an ideal reference to validate our algorithm. For a 3-D transversely isotropic

medium, 5 of the 21 elastic coefficients are independent, and if the symmetry axis is aligned with one of the axes of the grid, only 9 coefficients are nonzero. But after an arbitrary rotation, many of them become nonzero, thus validating the full algorithm. In addition, in a realistic geological model with curved layers, the symmetry axis, if any, would most likely not coincide with any grid axis.

We therefore study a homogeneous block of Mesaverde clay shale, whose five independent elastic coefficients for a vertical symmetry axis before rotation are given in Table 4. These parameters are taken from Thomsen (1986) and Carcione et al. (1992). The four other nonzero coefficients are $c_{22} = c_{11}$, $c_{55} = c_{44}$, $c_{23} = c_{13}$, and $c_{66} = (c_{11} - c_{12})/2$. The block has a size of 2500 m × 2500 m × 2500 m. All its edges are free surfaces. We rotate the vertical symmetry axis by 30° about the horizontal x-axis. General formulas for rotating the stiffness tensor expressed in reduced Voigt notation can be found in Helbig (1994, Appendix 3C). We place a force source inside the block at $x = 1250$ m, $y = 1562.5$ m, and $z = 937.5$ m. The force acts exactly along the symmetry axis. The time dependence of the source is a Ricker wavelet with dominant frequency $f_0 = 16$ Hz, and onset time $t_0 = 0.07$ s. The medium is discretized

FIG. 5. Snapshot of the displacement vector obtained with the SEM at time $t = 32\,\mu$s for a heterogeneous medium composed of a transversely isotropic zinc crystal with vertical symmetry axis (left) and an isotropic material (right). The area displayed in this closeup has a size of 34 cm × 34 cm. The vertical thick line represents the interface. The point source, indicated by the cross, is placed at a distance of 2 cm from the interface. The line of receivers is indicated by the dotted line between the two diamonds. The wavefronts show a very anisotropic shape, close to the one recorded for pure zinc (Figure 1), in the left part of the medium; in the right part, which is isotropic, the wavefronts are almost circular. This simulation is in good qualitative agreement with similar results computed in another study based upon the Fourier method (see Figure 5 in Carcione et al., 1988). Numerous reflected, transmitted, and converted phases can be observed (see the text and the snapshot in Figure 4 for more details).

Vertical displacement (60 μs)

FIG. 4. Snapshot of the FD experiment at time $t = 60\,\mu$s. The vertical component of displacement is displayed in grayscale levels. The displayed area is 68 cm × 64 cm. The vertical thick line represents the interface between the anisotropic (left) and isotropic (right) half spaces. The white circle indicates the position of the vertical point force. The dashed white line indicates the position of the 49 receivers used in Figure 6. Numerous phases, whose detailed description is given in Table 3, can be identified.

using a grid of $48 \times 48 \times 48$ spectral elements. We use a polynomial degree $N = 5$ within each element; therefore, the total number of points of the global grid is $(5 \times 48 + 1)^3 = 13\,997\,521$. The signal is propagated for 1 s using a time step of 0.5 ms in the explicit Newmark scheme, for a total of 2000 time steps. As underlined in Komatitsch and Tromp (1999) for the isotropic case, the 3-D SEM code is implemented on a parallel machine with distributed memory, based upon the Message Passing Interface (MPI), and a high parallel efficiency is obtained, which is one of the important features of the SEM.

Figure 8 shows a snapshot at time $t = 0.25$ s of the projection of the displacement field onto a 2-D (y, z) cutplane at $x = 1250$ m in the middle of the block. The qP and qSV wavefronts can be clearly observed, tilted by 30° from the vertical direction, as expected. In particular, the qSV wavefront exhibits four very clear cuspidal triangles, two of which propagate along the symmetry axis, and the two others in the perpendicular direction.

As shown by Carcione et al. (1992), for the Mesaverde clay shale, we can compute the analytical solution for the displace-

ment along the symmetry axis. Because of the symmetry, the only nonzero component is precisely the component along the symmetry axis. We therefore place a receiver on the symmetry axis, at a distance of 728.9 m from the source, as shown in Figure 8. In Figure 9, we plot the displacement computed using the SEM, as well as the analytical solution. The agreement is excellent, both for the qP wave around $t = 0.25$ s, and for the very strong qSV wave between $t = 0.4$ and $t = 0.5$ s, apart from a very small difference in the amplitude of the qSV wave. The weak signal present around $t = 0.65$ s is a wave reflected from one of the free surfaces of the block.

CONCLUSIONS

We have shown that the use of a spectral element method allows one to model wave propagation in fully anisotropic 2-D and 3-D elastic media, including in the presence of a free surface. The method provides high accuracy for 2-D test cases involving homogeneous transversely isotropic crystals with known analytical solutions. Strongly curved qP and qS wavefronts are well reproduced, including cuspidal triangles.
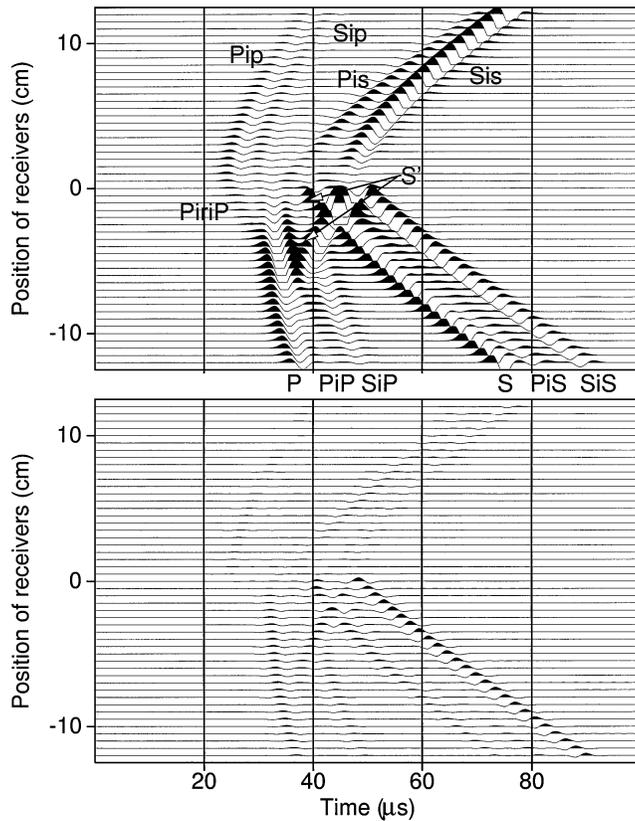
FIG. 6. Vertical component of displacement recorded at 49 receivers in the SEM simulation (top). The location of the receivers is indicated in Figures 4 and 5. In order to enhance the amplitude, the clipping factor is set to 1/8th of the maximum amplitude in each seismogram. The notation in Table 3 is used for identification of the main phases. The FD seismogram is not displayed because it is almost identical to the SEM result. Instead, we plot, at the same scale but without clipping, the difference between the seismograms computed with both methods, amplified by a factor of 5 (bottom). The small amplitude of these residuals clearly shows that the agreement between the two methods is excellent, except perhaps for the last phase in the anisotropic medium (SiS).

Table 3. Identification of the main phases present in the heterogeneous experiment. All these phases can be seen on the snapshot displayed in Figure 4. Those that are the most energetic can also be observed on the seismogram in Figure 6 and on the traces in Figure 7.

P	Direct qP-wave in the anisotropic medium
PiP	qP-wave reflected off the interface
PiS	qP-wave reflected off the interface and converted into a qS-wave
Pip	qP-wave transmitted as a P-wave into the isotropic medium
Pis	qP-wave transmitted as an S-wave into the isotropic medium
PiriP	qP-wave refracted in the isotropic medium along the interface and reflected into the anisotropic medium as a qP-wave
PiriS	qP-wave refracted in the isotropic medium along the interface and reflected into the anisotropic medium as a qS-wave
Pirip	qP-wave refracted in the isotropic medium and transmitted as a P-wave into the isotropic medium
S	Direct qS-wave in the anisotropic medium
S′	Part of the direct qS-wave (cuspidal zone) that arrives before the direct wave labeled S
SiS	qS-wave reflected off the interface
SiP	qS-wave reflected off the interface and converted into a qP-wave
Sis	qS-wave transmitted as an S-wave into the isotropic medium
Sip	qS-wave transmitted as a P-wave into the isotropic medium

Table 4. Independent elastic coefficients and density of the Mesaverde clay shale used in the 3-D validation tests, in the case of a symmetry axis aligned with the vertical axis of the grid. The elastic coefficients have to be multiplied by 10^9 to obtain values in N·m^{-2}. The density ρ is given in kg·m^{-3}. The other elastic coefficients are zero.

c_{11}	c_{12}	c_{13}	c_{33}	c_{44}	ρ
66.6	19.7	39.4	39.9	10.9	2590.
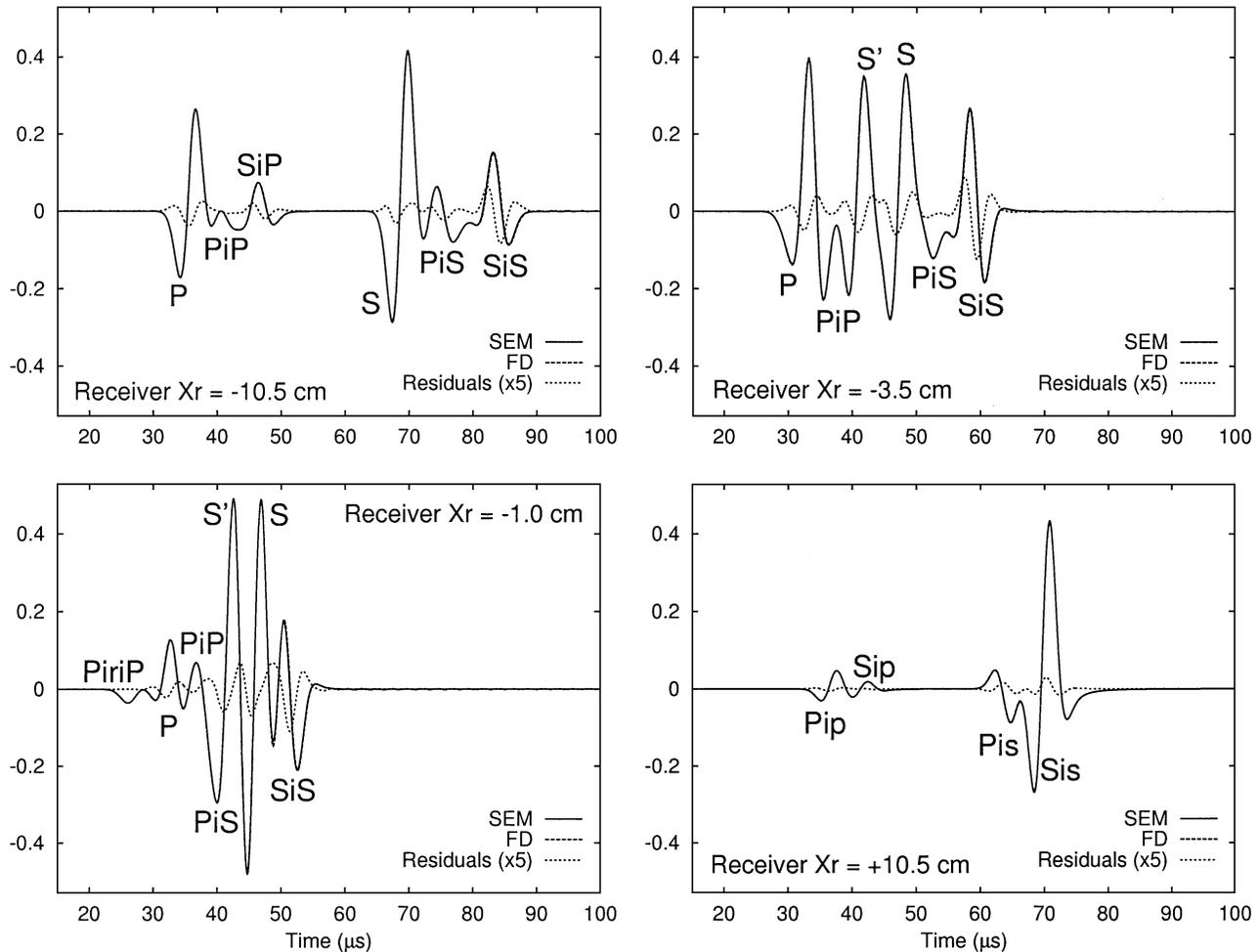
FIG. 7. Seismograms computed using the SEM for the heterogeneous numerical experiment displayed in Figures 4 and 5. The corresponding seismograms for all receivers are shown in Figure 6. We show four traces corresponding to receivers located at $x_r = -10.5$ cm, -3.5 cm, -1 cm, and $+10.5$ cm. The vertical component of displacement obtained using the SEM is illustrated by the solid line; that of the FD simulation is shown by the dashed line. As the two results are almost superimposed, the difference between the two, amplified by a factor of 5, is shown by the dotted line. For all phases in the four plots, the main part of the misfit is due to small time shifts. A description of the main phases is given in Table 3; they are also illustrated on the snapshot in Figure 4 and on the seismograms in Figure 6.

We have demonstrated that the method can also handle heterogeneous anisotropic models. We found good qualitative agreement with published results computed using a Fourier method, and excellent quantitative agreement with FD results. We have finally shown that the method can deal with fully anisotropic 3-D models, by studying a transversely isotropic 3-D medium with a tilted symmetry axis with respect to the axes of the computational grid. Excellent agreement with the analytical solution on the symmetry axis was found. Future work will focus on applying this method to more realistic structures, for instance regions with fractured rocks.

ACKNOWLEDGMENTS

REFERENCES

Backus, G. E., 1962, Long-wave elastic anisotropy produced by horizontal layering: J. Geophys. Res., **67**, 4427–4440.
Booth, D. C., and Crampin, S., 1983, The anisotropic reflectivity technique—Theory: Geophys. J. Roy. Astr. Soc., **72**, 755–766.
Canuto, C., Hussaini, M. Y. , Quarteroni, A., and Zang, T. A., 1988, Spectral methods in fluid dynamics: Springer-Verlag.
Carcione, J. M., Kosloff, D., Behle, A., and Seriani, G., 1992, A spectral scheme for wave propagation simulation in 3-D elastic-anisotropic media: Geophysics, **57**, 1593–1607.
Carcione, J. M., Kosloff, D., and Kosloff, R., 1988, Wave propagation simulation in an elastic anisotropic (transversely isotropic) solid: Q. J. Mech. Appl. Math., **41**, 319–345.
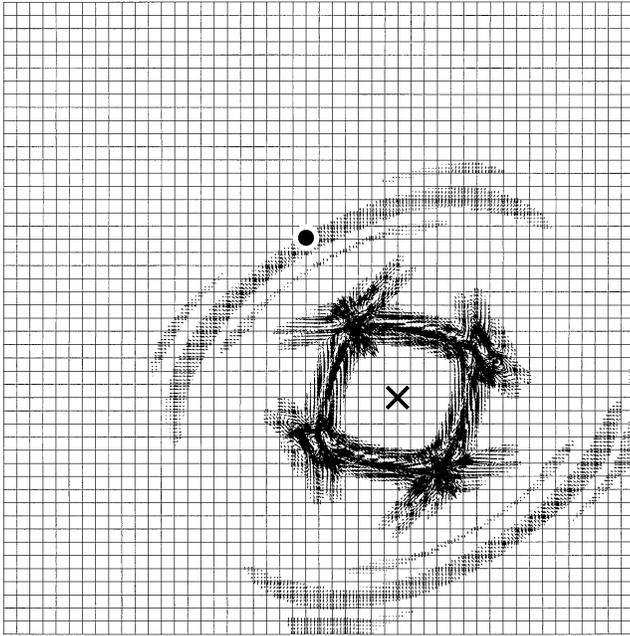
FIG. 8. Snapshot at time $t = 0.25$ s of the projection of the displacement vector onto a (y, z) cutplane at $x = 1250$ m in the middle of a block of Mesaverde clay shale. The symmetry axis of this 3-D transversely isotropic medium is tilted by $30°$ from the vertical direction in this cutplane. The displacement vector is represented at the Gauss-Lobatto-Legendre points of the mesh, which are nonevenly spaced. The source, indicated by the cross, is a force acting along the symmetry axis. The qP and qSV waves can be clearly observed. In particular, the qSV wave exhibits four noticeable cuspidal triangles. The dot indicates the position of the receiver on the symmetry axis at which the computed displacement is compared to the analytical solution in Figure 9.
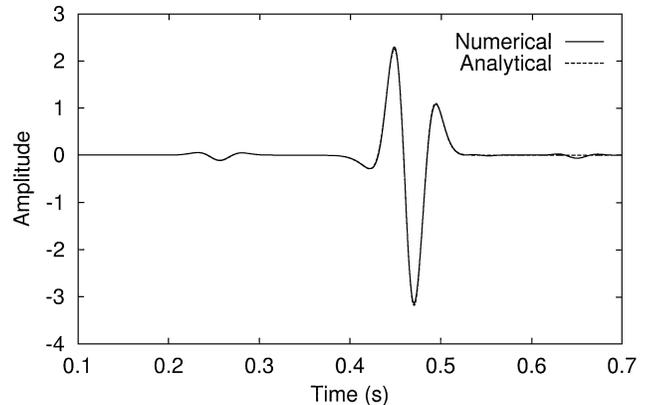
FIG. 9. Numerical (solid line) and analytical (dashed line) component of the displacement along the symmetry axis, at the receiver of Figure 8 in a block of Mesaverde clay shale with tilted symmetry axis, at a distance of 728.9 m from the source. The two other components are zero by symmetry. The agreement obtained is excellent both for the qP wave around $t = 0.25$ s, and for the strong qSV wave between $t = 0.4$ and $t = 0.5$ s. The small wave present around $t = 0.65$ s is a reflection from one of the free surfaces of the block (not accounted for in the analytical solution).

Carcione, J. M., and Wang, P. J., 1993, A Chebyshev collocation method for the wave equation in generalized coordinates: Comput. Fluid Dyn. J., **2**, 269–290.

Clayton, R., and Engquist, B., 1977, Absorbing boundary conditions for acoustic and elastic wave equations: Bull, Seis Soc. Am., **67**, 1529–1540.

Crampin, S., Chesnokov, E. M., and Hipkin, R. G., 1984, Seismic anisotropy—The state of the art II: Geophys. J. Roy. Astr. Soc., **76**, 1–16.

Dziewonski, A. M., and Anderson, D. L., 1981, Preliminary reference earth model: Phys. Earth Plan. Int., **25**, 297–356.

Faccioli, E., Maggio, F., Paolucci, R., and Quarteroni, A., 1997, 2D and 3D elastic wave propagation by a pseudo-spectral domain decomposition method: J. Seismology, **1**, 237–251.

Forsyth, D. W., 1975, The early structural evolution and anisotropy of the oceanic upper mantle: Geophys. J. Roy. Astr. Soc., **43**, 103–162.

Helbig, K., 1994, Foundations of anisotropy for exploration seismics, *in* Helbig, K., and Treitel, S., Eds, Handbook of geophysical exploration, section I: Seismic exploration: Pergamon.

Hughes, T. J. R., 1987, The finite element method, linear static and dynamic finite element analysis: Prentice-Hall International.

Igel, H., Mora, P., and Riollet, B., 1995, Anisotropic wave propagation through finite-difference grids: Geophysics, **60**, 1203–1216.

Komatitsch, D., 1997, Méthodes spectrales et éléments spectraux pour l'équation de l'élasto-dynamique 2D et 3D en milieu hétérogène: Ph.D. thesis, Institut de Physique du Globe.

Komatitsch, D., Barnes, C., and Tromp, J., 2000, Wave propagation near a fluid-solid interface: a spectral-element approach: Geophysics, **65**, 623–631.

Komatitsch, D., Coutel, F., and Mora, P., 1996, Tensorial formulation of the wave equation for modelling curved interfaces: Geophys. J. Internat., **127**, 156–168.

Komatitsch, D., and Tromp, J., 1999, Introduction to the spectral-element method for 3-D seismic wave propagation: Geophys. J. Internat., **139**, 806–822.

Komatitsch, D., and Vilotte, J. P., 1998, The Spectral element method: An efficient tool to simulate the seismic response of 2D and 3D geological structures: Bull, Seis Soc. Am., **88**, 368–392.

Komatitsch, D., Vilotte, J. P., Vai, R., Castillo-Covarrubias, J. M., and Sánchez-Sesma, F. J., 1999, The Spectral element method for elastic wave equations: Application to 2D and 3D seismic problems: Internat. J. Num. Method. Eng., **45**, 1139–1164.

Kosloff, D., Reshef, M., and Loewenthal, D., 1984, Elastic wave calculations by the Fourier method: Bull, Seis Soc. Am., **74**, 875–891.

Patera, A. T., 1984, A spectral element method for fluid dynamics: Laminar flow in a channel expansion: J. Comput. Phys., **54**, 468–488.

Payton, R. G., 1983, Elastic wave propagation in transversely isotropic media: Martinus Nijhoff.

Priolo, E., Carcione, J. M., and Seriani, G., 1994, Numerical simulation of interface waves by high-order spectral modeling techniques: J. Acoust. Soc. Am., **95**, 681–693.

Quarteroni, A., Tagliani, A., and Zampieri, E., 1998, Generalized Galerkin approximations of elastic waves with absorbing boundary conditions: Comput. Method. Appl. Mech. Eng., **163**, 323–341.

Robertsson, J. O. A., 1996, A numerical free-surface condition for elastic/viscoelastic finite-difference modeling in the presence of topography: Geophysics, **61**, 1921–1934.

Schoenberg, M., and Muir, F., 1989, A calculus for finely layered anisotropic media: Geophysics, **54**, 581–589.

Seriani, G., 1998, 3-D large-scale wave propagation modeling by spectral element method on Cray T3E multiprocessor: Comput. Method. Appl. Mech. Eng., **164**, 235–247.

Seriani, G., Priolo, E., Carcione, J. M., and Padovani, E., 1992, High-order spectral element method for elastic wave modeling: 62nd Ann. Internat. Mtg., Soc. Expl. Geophys., Expanded Abstracts, 1285–1288.

Seriani, G., Priolo, E., and Pregarz, A., 1995, Modelling waves in anisotropic media by a spectral element method, *in* Cohen, G., Ed., Third international conference on mathematical and numerical aspects of wave propagation: Soc. Ind. Appl. Math., 289–298.

Tarnow, N., and Simo, J. C., 1994, How to render second-order accurate time-stepping algorithms fourth-order accurate while retaining the stability and conservation properties: Comput. Method. Appl. Mech. Eng., **115**, 233–252.

Tessmer, E., 1995, 3-D seismic modelling of general material anisotropy in the presence of the free surface by a Chebyshev spectral method: Geophys. J. Internat., **121**, 557–575.

Thomsen, L., 1986, Weak elastic anisotropy: Geophysics, **51**, 1954–1966.

White, J. E., 1982, Computed waveforms in transversely isotropic media: Geophysics, **47**, 771–783.